# Biodegradable PMMA coated Zn–Mg alloy with bimodal grain structure for orthopedic applications - A promising alternative

Alia A. Diaa [a,b], Nahed El-Mahallawy [a,b], Madiha Shoeib [c], Flavien Mouillard [d], Tom Ferté [d], Patrick Masson [d], Adele Carradò [d,*]

[a] Design and Production Engineering Department, Faculty of Engineering, Ain Shams University, Cairo, 11517, Egypt
[b] Department of Design and Production Engineering, Faculty of Engineering and Materials Science, German University in Cairo, Cairo, 11835, Egypt
[c] Central Metallurgical Research and Development Institute, El Tebbin, Cairo, 11722, Egypt
[d] Institut de Physique et Chimie des Matériaux de Strasbourg, IPCMS, UMR 7504 CNRS, Université de Strasbourg, 67000, Strasbourg, France

## ABSTRACT

The study examines the impact of microstructure and polymethyl methacrylate (PMMA) grafting on the degradability of Zn–Mg alloys. The mechanical properties of a Zn alloy containing 0.68 wt% Mg and extruded at 200 °C are enhanced for degradable load-bearing applications, addressing a crucial need in the field. The material exhibits a bimodal grain size distribution that is random texture, consisting of secondary phases, grains, and sub-grains. With an elongation to failure of 16 %, the yield and ultimate tensile strengths are 325.9 and 414.5 MPa, respectively, and the compressive yield strength is 450.5 MPa.

The "grafting-from" method was used to coat a few micrometers thick of PMMA on both bulk and scaffold Zn alloys to mitigate the corrosion rate. The last one is a porous structure, with a porosity of 65.8 %, considered as in the first approach of an orthopedic implant. After being immersed for 720 h, the PMMA-grafted bulk alloy's corrosion rate decreased from 0.43 to 0.25 mm/y. Similarly, the scaffold alloy's corrosion rate reduced from 1.24 to 0.49 mm/y. These results indicate that the method employed could be used for future orthopedic applications.

## 1. Introduction

### 1.1. Biodegradable alloy design and thermomechanical processing

Numerous investigations have been conducted to develop biomedical materials to fabricate temporary implants intended to replace damaged hard tissue, aiming to prevent the need for a subsequent surgical procedure for implant removal [1]. Metals are more amenable to being employed as biodegradable materials for orthopedic purposes than other engineering materials [2]. Magnesium is considered a very important macromineral because of its essential nutritional value and wide range of physiological functions in the body [3]. However, its implementation in biomedical materials is impeded by practical challenges [1,2]. Magnesium exhibits an exceptionally rapid corrosion rate and generates hydrogen bubbles during degradation, which can compromise the structural integrity of newly formed bones [4].

Zinc, classified as a micromineral following Mg [4], displays a moderate degradation rate and no potentially hazardous reaction by-products [3]. In its pure form, Zn presents inadequate mechanical properties (ultimate tensile strength (UTS) $\cong$ 100–150 MPa and elongation to failure ($E_f$) $\cong$ 0.3–2 %), which fall short of meeting the requirements for an orthopedic implant application (UTS $\geq$300 MPa and $E_f \geq$ 15 %) [5,6]. Zn alloy with minimal amounts of Mg is believed to fulfill the need to balance the nutritional benefits of Mg and the practical considerations of material performance [6]. Thermomechanical processing, following casting, can enhance mechanical performance by enhancing solute atom dissolution and breaking down detrimental secondary phases by inducing diffusion kinetics, high dislocation densities, and shear stresses [7]. During thermomechanical processing, the combination of elevated temperatures and mechanical deformation leads to the activation of dynamic recrystallization mechanisms. This phenomenon involves the nucleation and growth of new grains within the deformed matrix, which helps relieve stored energy and reduce the dislocation density [7,8].

Ye et al. [9] implemented a rotary-die equal-channel angular pressing approach on a Zn-0.1 Mg alloy, achieving a highly refined grain structure (1.14 $\pm$ 0.22 μm), weak texture, and nanoscale Mg–Zn metallic phases within the grains. This microstructure led to UTS of 383 MPa and $E_f$ of 45.6 %. Li et al. [10] successfully developed a heterogeneous microstructure of the Zn–1Mg alloy through traditional extrusion,

---

resulting in coarse grains of approximately 6.84 μm and fine grains of around 1.65 μm. They argued that this grain refinement, combined with precipitation strengthening and the activation of non-basal slip systems, yielded a UTS of 320 MPa. Li et al. [10] also asserted that the coarse grains contribute to a high ductility of 32 %. In another study, Lou [11] employed the conventional extrusion process to moderate the texture of the Zn-0.2Mg-0.8Mn alloy and attain fully recrystallized grains with an average size of 2 μm, aiming to strike a balance between high strength and ductility. The strengthening effects of grain boundaries, second-phase precipitates, and non-basal texture led to UTS of 330–350 MPa and $E_f$ of 33 %.

Surface and microstructural features help predict corrosion mechanisms and offer insights into product formation. Adding a soluble alloying element shifts open-cell corrosion potential. Depending on the secondary phases, corrosion can be uniform or localized micro-galvanic [10]. Post-thermomechanical processing is believed to positively influence corrosion behavior by refining grain structure, ensuring broad and uniform chemical distribution, and facilitating the dispersion of second-phase precipitates [12–14].

Using biodegradable metals in orthopedic scaffolds is a challenge, as noted in Refs. [15,16]. Scaffolds must be porous to facilitate bone growth and degrade at a rate that matches the healing process of bone. Xia et al. [16] have demonstrated the detrimental impact of porosity on these scaffolds' mechanical strength and biodegradation performance. They conducted a comparative study on the compressive strength and corrosion rate of pure Zn in two states: in its bulk form after extrusion and in a porous state manufactured by laser powder bed fusion with a strut size of 600 μm and pore size of 400 μm. The results revealed that the compressive yield and ultimate strengths of the bulk metal were 25.1 ± 1.6 MPa and 169.9 ± 2.5 MPa, respectively, whereas for the scaffolds, they were 14.9 ± 1.8 MPa and 49.2 ± 2.1 MPa, respectively. Additionally, the corrosion rate for the bulk state was 0.25 ± 0.01 mm/y, whereas it increased to 1.09 ± 0.02 mm/y for the scaffold.

### 1.2. Surface modification techniques for improving biodegradable metal performance

Polylactic acid (PLA), polyglycolic acid (PGA), and polycaprolactone (PCL) stand out for their commendable biodegradability and osteoconductivity [17]. They have been developed as coatings to control the degradation affinity of metals [18]. Polymethyl methacrylate (PMMA), a lightweight polymer with no taste or odor, has proven biocompatible [19]. Accordingly, PMMA became amenable as a bioactive, non-resorbable polymer for bone regeneration and drug delivery applications [19–22]. Barua et al. [21] prepared a HA (hydroxyapatite)/PMMA/ZnO composite-based scaffold for curing segmental orthopedic defects. They tested the scaffold's cytotoxicity by XTT assay seeding human osteosarcoma, followed by incubation and 450 nm absorbance measurement, which shows enhanced optical density and cell viability of the scaffold. Son et al. [23] developed a PCL/PMMA fibrous scaffold implanted in a rat skull. They found that adjacent to the scaffold, orthopedic tissues typical to the initial ones are regenerated with no unfavorable body reaction. In another study, Jayaram et al. [22] employed PMMA for the controlled local liberation of zoledronic acid to enhance bone mineral density and reduce bone pain associated with metastatic bone disease.

Spin-coated PMMA has effectively slowed the corrosion rate of biodegradable Mg alloys while encouraging suitable cell attachment and viability [24,25]. As a spin-coating method, sol-gel deposition forms weak bonds (such as van der Waals forces) between the polymer and the metal, relying on superficial physical attachment. In contrast, the "grafting-from" technique establishes a robust chemical bond between the polymer and the substrate. Diaa et al. [26] applied the "grafting-from" technique to bond PMMA chains on the surface of the Zn-1.89 Mg alloy. The grafted PMMA acts as a protective layer, mitigating severe corrosion in highly included eutectic phases and transforming aggressive localized corrosion (galvanic and pitting) into delayed crevice corrosion, resulting in minute pitting in the α-Zn phase. Elaborating on this, the application of the PMMA protective layer on metals, such as titanium in Ref. [27] and Zn-1.89 Mg in Ref. [26], involved a three-stage "grafting-from" technique: (i) alkali treatment, (ii) initiation using bromoisobutyrate-undecyl-1-phosphonic acid ($C_{15}H_{30}O_5PBr$), and (iii) the development of the polymeric chain by atom transfer radical polymerization (ATRP) [28,29]. This three-stage "grafting-from" process created a protective PMMA layer with a few micrometers thickness, forming a strong covalent bond adhesion to the substrate [30].

To obtain biodegradable materials useable in orthopedic applications, the current study endeavors to establish (i) the synergy among alloy design and post-thermomechanical processing to achieve the benchmark strength and ductility and (ii) the surface modification to obtain the required degradation rate. The study was performed on Zn-0.68 Mg alloy in bulk and scaffold form with a designed porosity of 65.8 % of the total volume. To highlight the benefits of extrusion-induced strengthening alloy, a PMMA was grafted as corrosion inhibition.

## 2. Materials and methods

### 2.1. Fabrication of Zn-0.68 Mg alloy rods and Zn-0.68 Mg alloy scaffolds

Zn–Mg alloy was produced by casting it in an electric resistance furnace at a temperature of 500 °C using Zn ingots with a purity of 99.99 % and Mg ingots with a purity of 99.99 %. To limit the oxidation and evaporation of Zn and Mg, melting was carried out under an Ar 0.5 % $SF_6$ gas mixture flow with a rate of about 2 L/h. The weight ratio of added Zn to Mg was 98:2. However, the obtained weight percentage of Mg in the alloy determined via inductively coupled plasma-atomic emission spectrometry (ICP-AES Varian 715-Es, USA) was detected to be 0.68, and Zn is balanced (alloy nominal composition is Zn-0.68 Mg).

Stirring before pouring was applied for about 5 min using a graphitic rod to ensure homogenization in the chemical composition of the alloy. The melt was poured into two steel cylindrical molds preheated to 200 °C, each 45 mm in diameter and 70 mm in length. The cast ingots were cooled at room temperature. Afterward, the ingots underwent an 8-h heat treatment at 350 °C followed by water quenching. After casting and heat treatment, surface machining was used to remove about 1 mm of the ingot diameter as an anoxidized layer. Afterward, single-step direct extrusion was carried out on a 100-tons hydraulic press at a temperature of 200 °C with an extrusion speed of 4 mm/s. The obtained rods after extrusion were 11 mm in diameter, achieving an extrusion ratio of ~16:1 (ratio of the rod cross-sectional area before and after extrusion).

The extruded rods were machined to cubic shapes ($7 \times 7 \times 7$ mm$^3$) and then perforated using a fine milling technique to fabricate the Zn-0.68 Mg alloy scaffold. Perforation was operating at 6000 rpm and a 100 mm/min feed rate using a mineral oil-based cooling fluid introduced at a flow rate of 2 mL/h. The perforation process resulted in 2D interconnected channels, with each channel formed due to a through-all hole with a 1 mm diameter. The distance between each two successive holes is 0.75 mm. The obtained scaffolds are of 65.8 % designed porosity with a skeletal-shaped unit cell of 0.755 ± 0.025 mm strut size.

### 2.2. Surface preparation of Zn-0.68 Mg alloy

In preparation for mechanical testing, PMMA-grafting, corrosion testing, and microstructural investigations, the surfaces were gradually refined, grinding until P4000 grit SiC abrasive paper. Subsequently, they were polished using diamond paste (1PS4, ESCIL). Specimens were subjected to sequential ultrasonic cleaning cycles in this specific order: cyclohexane, acetone, ethanol, and deionized water, with each solvent treatment lasting 10 min in a 100 mL beaker to ensure cleanliness. No drying process was used as the samples were placed in water for the following steps. Specimens for electron backscatter diffraction (EBSD)

analyses underwent initial preparation via conventional grinding and subsequent diamond polishing until a roughness of 0.5 μm. Afterward, precision ion milling was conducted using an $Ar^+$ ion polishing system (PIPS, Gatan). The operational parameters included an accelerating voltage of 3 kV and an incident angle of 3°, maintained under a liquid-nitrogen cooling system.

## 2.3. Deposition of PMMA coating

The PMMA coating application was executed using the "grafting-from" technique, following a three-step procedure outlined by Reggente et al. [27]. In the activation step, cubic dense and cubic scaffold samples were suspended in a Teflon beaker using Teflon wire and immersed in a 5 M sodium hydroxide (NaOH) solution at 80 °C for 1 h. Subsequently, the samples were rinsed with deionized water. The functionalization step followed immediately. The samples were dipped in an aqueous solution of 2 mM bromoisobutyrate-undecyl-1-phosphonic acid at 95 °C without light for 24 h. Afterward, the functionalized samples were cleaned in a dichloromethane and deionized water ultrasonic bath for 10 min. The ATRP was achieved by dipping the samples in a reactor for 24 h at 35 °C under an Ar atmosphere. The reactor underwent thorough purging to remove residual air through three cycles of argon-vacuum. The following reactives were added under stirring: 39 mg of copper bromide (Cu(I)Br) (Sigma Aldrich, 98 %), 18 mL of anisole (Acros Organics, 99 %), and 48 μL of pentamethylene diethyl-triamine (PMDETA)

ASTM G5-87 guidelines [35] were followed for the electrochemical test, employing a potentiostat/galvanostat apparatus (Autolab, Metrohm, USA) equipped with Nova 10.11 software for data analysis. The reference electrode was Ag/AgCl, and a Pt electrode was the counter electrode. A mirror-like surface of the cubic shape specimen was prepared by grinding and polishing to serve as the working electrode, with an exposed surface area of 19.6 mm². The open circuit potential (OCP) was set up in the range of −400 mV–600 mV, with a scan rate of 1 mV/s. EIS was carried out across a frequency range from 100 mHz to 100 kHz, using a sinusoidal voltage signal with an amplitude of 10 mV.

The samples used for the static immersion tests were in the shape of discs with 11 mm diameter and 1 mm thickness, had mirror-like surfaces, and were hung with a Teflon thread through a 1 mm hole in the desk. The test was conducted following the ASTM-G31-72 [36] standard. SBF volume to sample surface area ratio was approximately 2000–4000 mL/mm². The specimens were weighed both before and after immersion. The corrosion rate was calculated at distinct periods: 6, 24, 120, 240, 480, and 720 h of immersion. An incubator was used to preserve the temperature of the solution at 37.0 ± 0.5 °C throughout the whole test period. It has to be noted that a different sample with its solution was used for each test duration. The corrosion products were removed by gentle mechanical brushing.

The corrosion rate was calculated in terms of weight loss, corrosion exposed surface area (either the lateral area of the disk or the lateral area of the scaffold plus the inner areas of the inner channels), the exposure

$$Corrosion\ rate\ (mm/y) = \frac{8.76 \times 10^7 \times weight\ loss\ (g)}{surface\ area\ cm^2 \times exposure\ period\ h \times density (gm/cm^2)} \qquad \text{eq.(1)}$$

(TCI, 99 %). 18 mg of malononitrile (TCI, 98 %) was involved in improving the polymerization process. Lastly, 22 mL of methyl methacrylate (MMA) (Acros Organics) was included after the elimination of its stabilizer by flowing through a pad of basic aluminum oxide (Acros Organics). After polymerization, the samples were cleaned in an ultrasonic bath with deionized water to remove unreacted monomers and residual catalytic materials.

## 2.4. Mechanical tests

Tensile and compression tests were conducted using a universal testing machine (Zwick AG-100KN ProLine, Germany) operating at ambient temperature at a strain rate of 0.001 s$^{-1}$. These mechanical tests were carried out according to the ASTM E8/E8M − 08 and ASTM E9-89a standards [31–33]. The tensile specimens were prepared following ASTM 8E guidelines, with a gauge length of 25 mm. On the other hand, compression tests were performed on cubic samples 7 × 7 × 7 mm³. Notably, both tensile and compression tests were conducted with loading applied along the same axis as the extruded cylinders. The compression tests of the scaffolds were carried out using a Lloyd testing machine (2 ton- LS100 Plus, UK) equipped with Nexygen software for data acquisition at a speed of 0.5 mm/min. The yield strength (YS$_{0.2\ \%}$) was determined from the load/displacement plot, considering a 0.2 % plastic deformation strain.

## 2.5. Electrochemical and static immersion corrosion tests

Electrochemical assessments, including potentiodynamic polarization, electrochemical impedance (EIS), and static immersion corrosion tests, were conducted under controlled conditions at 37.0 ± 0.5 °C in simulated body fluid (SBF) solution of 7.4 pH, prepared following the procedure outlined in Ref. [34].

period, and density of the material as represented in Equation (1) [36]:

## 2.6. Surface and cross-section characterizations

The alloy's phase analysis was conducted using an X-ray diffractometer ((XRD), Brucker D8 Advance, Germany) with Cu Kα radiation of 1.54 Å wavelength, operating at a tube voltage of 40 kV and tube current of 100 mA developing a 4°/min scanning rate and 0.02° step size. Phase quantification was performed by performing a Rietveld refinement analysis.

The Zn–Mg alloys grafted with PMMA were investigated using Fourier transform infrared (FTIR) spectroscopy PerkinElmer Spectrum Two, Waltham, USA), in the attenuated total reflectance (ATR) mode with a resolution of 4 cm$^{-1}$.

The surface composition and morphology of the PMMA samples and the corroded specimens were investigated using a scanning electron microscope (SEM) - JSM-6700 F, JEOL, Tokyo, Japan. This SEM was configured to employ backscattered electron information and was equipped with an energy-dispersive X-ray spectrometer (EDX).

To investigate the Zn-0.68Mg/PMMA interface, the edges of the specimens were ground and then coated with copper through plasma deposition. Subsequently, they underwent ion beam cross-polishing (Hitachi IM4000+, Japan). An argon-ionized plasma with a current of 130 μA was employed as the ion beam. This preparation examined the cross-sections using the Zeiss Geminis SEM 500, Oberkochen, Germany. The copper layer produced a distinct signal compared to the PMMA, facilitating the determination of PMMA thickness. Linear analysis was performed to ascertain the elemental compositions of the various layers.

## 2.7. Texture analysis

EBSD was employed for texture analysis using the FEI Quanta 400f instrument, which operates at 20 kV, from FEI/Japan. This technique allowed for the investigation of crystallographic orientation, and as a result, inverse pole figure (IPF) maps were generated. In these IPF maps, colored grains corresponded to the same code as in the stereographic triangles. Data processing was performed using the OIM TSL EBSD software.

## 2.8. Sample selection and testing statistical analysis

Three samples were considered for each characterization technique. Any test yielding a quantitative value was performed using a sample size of n = 3 for every specimen group, enabling the determination of the mean alongside its corresponding standard deviation.

## 3. Results

### 3.1. Microstructure and texture analysis

Fig. 1a and **b** shows the microstructure of the as-extruded Zn-0.68 Mg alloy after SEM/EDS and XRD analysis. According to size classification, the SEM images reveal a homogenous bimodal grain structure spanning the entire surface. The grains could be classified into relatively large grains surrounded by considerable areas of sub-grains. Two morphologies of secondary phases were also detected: minuscule precipitates within the grains and some small regions displaying a lamellar morphology that are believed to be $\alpha$-Zn + $Mg_2Zn_{11}$ eutectic structures. As shown in Fig. 1c, the XRD revealed the presence of two phases: the $\alpha$-Zn and the $Mg_2Zn_{11}$ phase, constituting approximately 6 % by volume.

A further investigation was conducted using EBSD, as depicted in Fig. 2, to reveal grain size and shape, the misorientation of the grain boundaries, and grains crystallographic orientations of the as extruded Zn-0.68 Mg alloy. The EBSD analysis displays the bimodal grain structure, Fig. 2a, where the microstructure comprises sub-grains with a globular morphology and coarse grains aligned with the extrusion

direction. Fig. 2a highlights two distinct regions to demonstrate the bimodal grain structure. **Region 1** encompasses a dense concentration of precipitates (no indexed black points) surrounded by tiny grains exhibiting a high degree of randomness in crystallographic orientation. This region demonstrates the pinning effect of the precipitates, impeding grain boundary migration and facilitating dynamic recrystallization. **Region 2** displays a non-recrystallized grain with a relatively large size and a discernible gradient of red color, indicating a propensity for crystal orientation variation within individual grains. Generally, the coarse grains have an average size of 10.1 ± 2.9 μm, while the sub-grains resulting from the dynamic recrystallization represent 48 % of the structure with an average size of 1.8 ± 1.0 μm, Fig. 2b.

Fig. 2c and d offer a detailed analysis of the nature of grain boundaries. It becomes evident that the predominant type of grain boundaries is the high-angle grain boundaries (HAGB), as indicated by the blue lines in the grain boundaries map, Fig. 2c. The HAGBs feature misorientation angles surpassing 15° and indicate recrystallized grains (as denoted by the blue lines in **Region 1**, Fig. 2c). The grain boundary misorientation map (Fig. 2c) depicts the other grain boundaries by red and green lines. These grain boundaries represent the low-angle grain boundaries (LAGB), characterized by misorientation angles below 15°. The LAGBs serve as indicators of grains retaining high energy levels due to their inability to undergo recrystallization; this was displayed by the sub-grains of LAGBs mismatch with the adjacent α-Zn matrix that tended to be formed inside the large grain (**Region 2**, Fig. 2e). The distribution of misorientation angles, depicted in Fig. 2d, reveals that 34 % of grain boundaries are LAGBs. Another intriguing observation is the presence of high-intensity peaks at misorientation of 85–90°, signifying the existence of {1 0 −1 2} <1 0 −1 1> twins. Notably, these twins, while not discernible on the microscale in Fig. 1a–b [42], are identified in the misorientation angle analysis of the grains.

The Kernel Average Misorientation (KAM) map is presented in Fig. 2e to indicate regions with significant strain fields in the ideal crystal lattice structure. The detected green lines indicate the stored slip dislocations in these areas [37]. From **Region 1** in Fig. 2e, it could be deduced that the precipitates surrounding the fully recrystallized sub-grains are free of strain fields. **Region 2** shows a typical
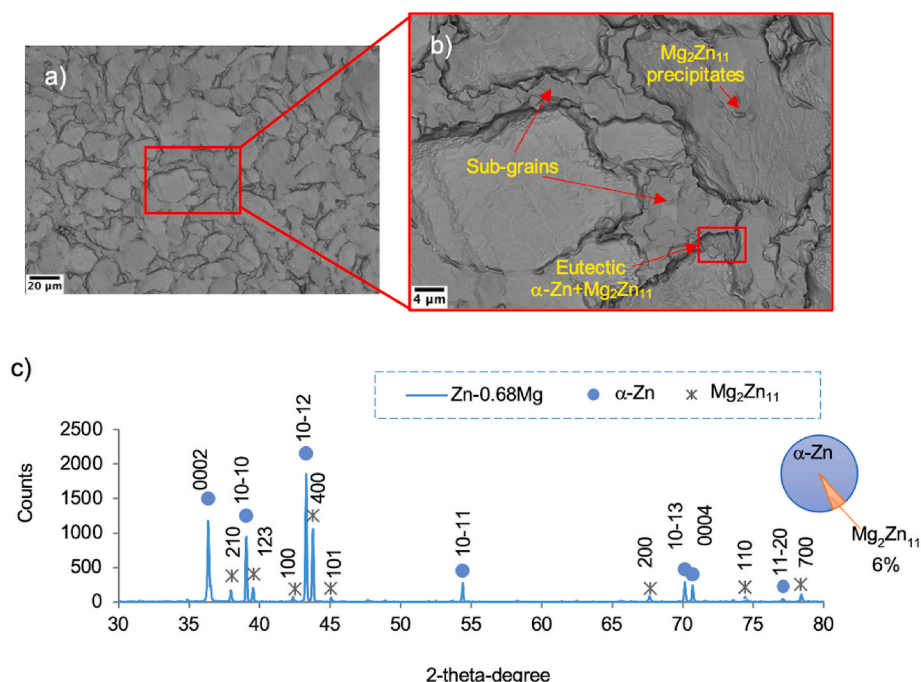


**Fig. 1.** Microstructure investigation of the as-extruded Zn-0.68 Mg alloy, (a) SEM of the cross-sectional surface, (b) a magnified view of (a) and (c) XRD analysis.
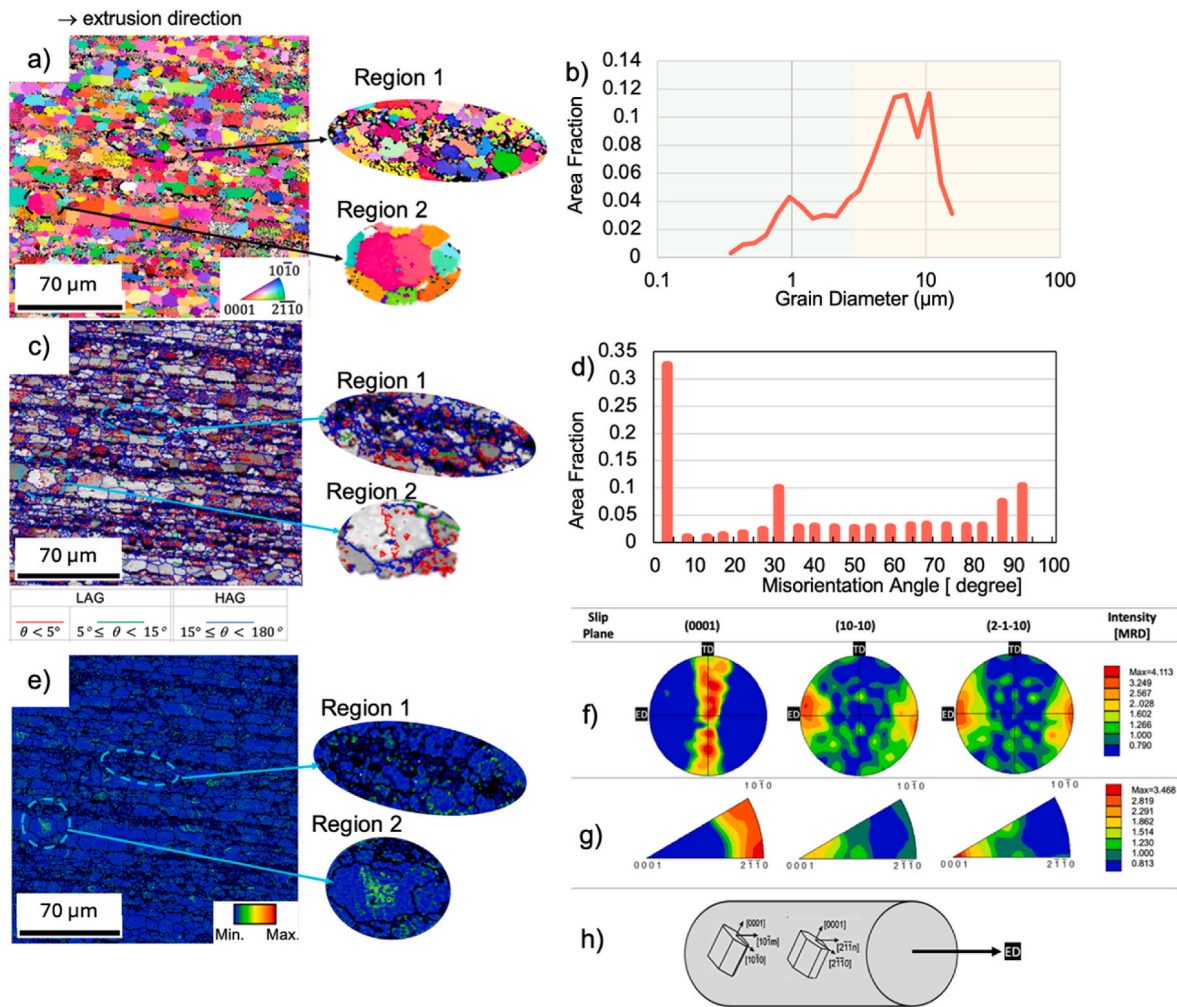
**Fig. 2.** EBSD investigation for the longitudinal surface of the as-extruded Zn-0.68 Mg alloy: (a) IPF maps, (b) grain size distribution, (c) high-low angle grain boundaries map, (d) misorientation angle distribution, (e) Kernel Average Misorientation map, (f) pole figures, (g) inverse pole figures for the (0001), (10-10) and (2-1-10) planes, and (h) a schematic representation of the pyramidal slip system. Note that ED is for extrusion direction, and [MRD] is for multiples of random distribution.

un-recrystallized coarse grain, including a small precipitate of secondary phases surrounded by a high density of strains due to the presence of dislocations.

The colors of the grains in the IPF maps, shown in Fig. 2a, correspond to the crystallographic c-axes of the hcp grains as indicated in the accompanying stereographic triangle. The IPF noted that the alloy's texture exhibits a stochastic distribution of grains devoid of regular orientations, reflecting the intrinsic randomness inherent in its microstructure. As shown in Fig. 2 (f-h), the crystallographic orientation of grains can be characterized by a weak basal fibrous texture. This characterization is because the (0001) basal plane, aligned parallel to the extrusion direction, exhibits a low intensity of 4.11 MRD (multiple of random distribution). The prevalence of the pyramidal slip system is supported by the nearly equal distribution of the <10-10> and <2-1-10> orientations along the extrusion direction.

### 3.2. Mechanical performance

The mechanical performance of both the bulk material and the porous structure of the as-extruded Zn-0.68 Mg alloy was assessed through room temperature tensile and compression tests. Fig. 3a illustrates the tensile engineering stress versus strain curves of bulk materials, and the related data are stated in Table 1. The tensile curves exhibit a minimal "strain softening" effect and an absence of necking strain,

indicating the entire elongation until failure occurs uniformly. After extrusion, the alloy recorded a UTS of 414.5 $\pm$ 17.6 MPa and a tensile strain to failure ($E_{f(T)}$) of 16.3 $\pm$ 2.7 %. The fractured surface analysis carried out by SEM analysis, Fig. 3b, shows a typical morphology of ductile fracture comprising lots of dimples and microcavities formed along with very small necking thickness reduction represented by the light fringe surrounding the fracture surface (insert at the upper right corner). On the other side, all the compression curves for the bulk material, as shown in Fig. 3c, exhibited higher strength values than the tensile curves. The compression curves of the bulk structure displayed continuously increasing stresses as the strains increased, with no significance for a failure point. However, a very slight macro barreling was noticed in the species. The average ultimate compression strength (UCS) and compressive strain to failure ($E_{f(c)}$) were detected to be 543.4 $\pm$ 57.5 MPa and 14.0 $\pm$ 3.4 %, respectively.

The yield compression strength ($YCS_{0.2\ \%}$) and the yield tensile strengths ($YTS_{0.2\ \%}$) of the bulk material were found to be 450.5 $\pm$ 47.6 and 325.9 $\pm$ 8.7 MPa, respectively, resulting in a compression to tension yield asymmetry of 1.38. In the case of porous structures, compression led to noticeable failure, represented by horizontal or diagonal cracks in the struts. The porous structures exhibited early yield at a stress of approximately 31.7 MPa, Fig. 3d, with the maximum withstood strain before failure reaching 173.3 $\pm$ 14.0 MPa, and the failure was observed at an average strain of about 0.2 %.
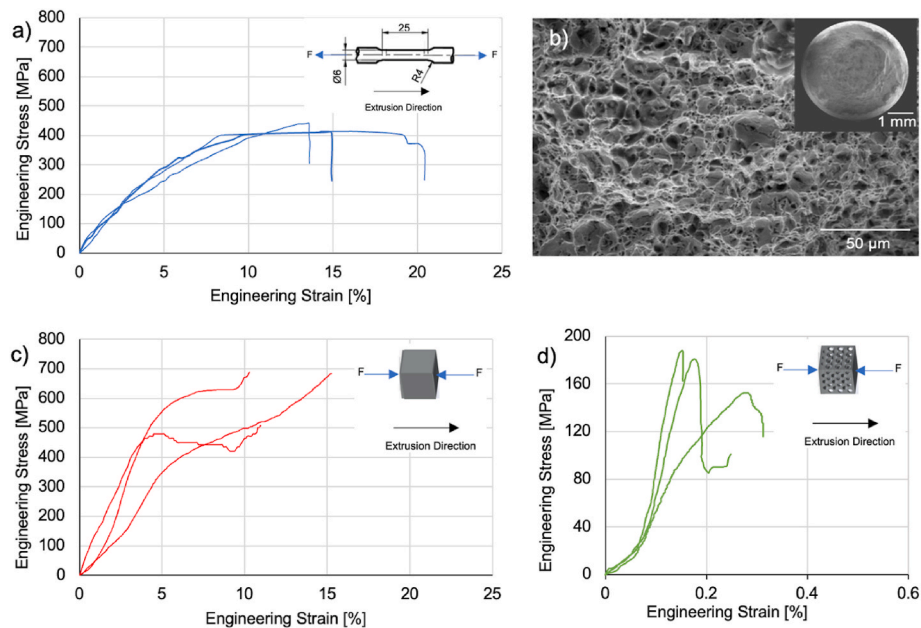
**Fig. 3.** Mechanical performance of the Zn-0.68 Mg alloy in its bulk and porous forms: a) tensile stress-strain curves of the bulk structure, b) morphology of the tensile fracture of the bulk structure, c) compression stress-strain curves for the bulk structures, and d) compression stress-strain curves for the porous structures. The inserts at the upper right corner of (a), (c), and (d) represent the specimen shape and the applier load direction to the extrusion direction.

**Table 1**
The mechanical performance of the bulk material and porous structure, where UTS is the ultimate tensile strength, $YTS_{0.2\%}$ is the yield tensile strength, $E_{f(T)}$ is the tensile strain to failure, UCS is the ultimate compressive strength, $YCS_{0.2\%}$ is the yield compressive strength and $E_{f(C)}$ is the compressive strain to failure.

| Tensile test (bulk material) | | | Compression test (bulk material) | | | Compression to tension yields asymmetry (bulk material) | | Compression test (porous structure) | |
|---|---|---|---|---|---|---|---|---|---|
| UTS [MPa] | $YTS_{0.2\%}$ [MPa] | $E_{f(T)}$ [%] | UCS [MPa] | $YCS_{0.2\%}$ [MPa] | $E_{f(c)}$ [%] | $YCS_{0.2\%}/YTS_{0.2\%}$ | UCS [MPa] | $YCS_{0.2\%}$ [MPa] | $E_f$ [%] |
| $414.5 \pm 17.6$ | $325.9 \pm 8.7$ | $16.3 \pm 2.7$ | $543.4 \pm 57.5$ | $450.5 \pm 47.6$ | $14.0 \pm 3.4$ | 1.38 | $173.7 \pm 14.0$ | $31.5 \pm 7.6$ | 0.2 |
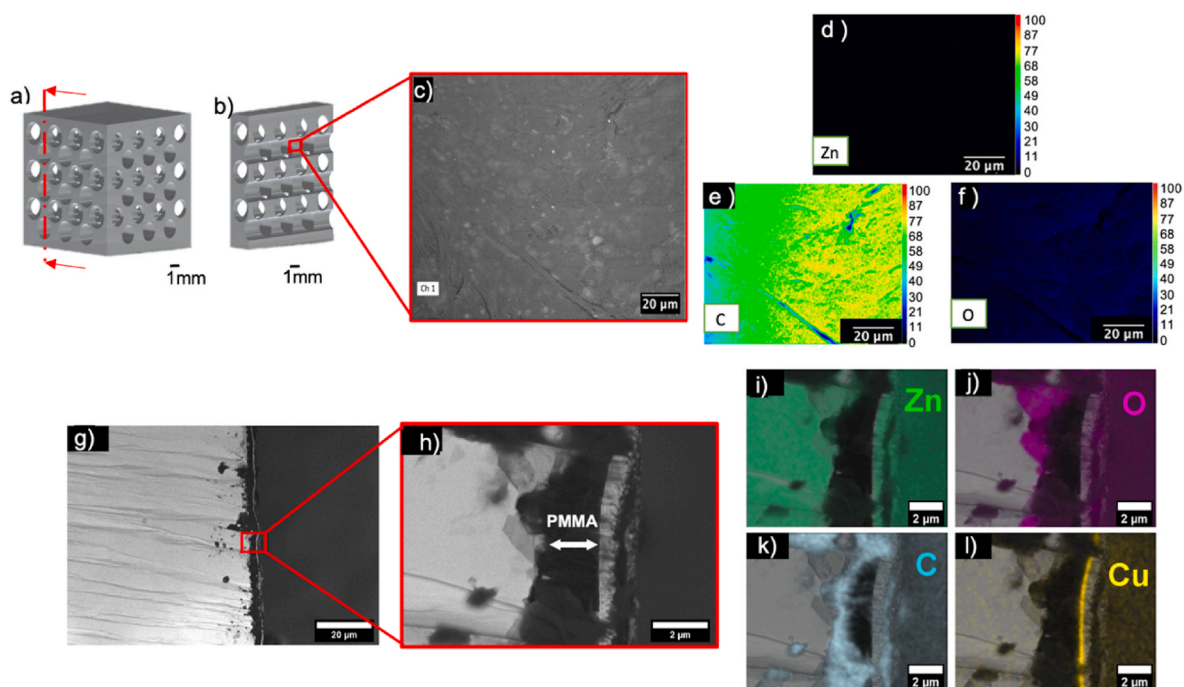


**Fig. 4.** PMMA coating investigation in scaffold channels, (a) a schematic representation of the scaffold, (b) cross-sectional scheme of the scaffold indicated in (a), (c) SEM micrograph of the coated channel, (d–f) EDX elemental mapping corresponding to SEM in (c), (g) cross-sectional examination of the PMMA coating; (h) magnified window; and (i–l) elemental mapping of SEM image (g), displaying the presence of Zn in green, C in purple, O in red, and Cu in yellow.

### 3.3. PMMA grafting

PMMA grafting on bulk and porous materials was accomplished through three steps: alkali treatment, grafting of an initiator, and polymerization. The alkali treatment aims to create hydroxyl groups (OH) on the alloy's surface and modify it by the formation of a porous structure. These chemical and morphological changes on the alloy's surface facilitate grafting, while the porosity enables columnar polymerization [29]. Grafting is achieved by immersing the alloy surface in the bromoisobutyrate-undecyl-1-phosphonic acid initiator ($C_{15}H_{30}O_5PBr$). It is crucial to note that the presence of the eleven-hydrocarbon ($C_{11}H_{22}$) spacer between the phosphonate group and the reactive α-bromo ester group is a must to ensure the stability of the molecule [27,38]. The phosphonic acid function reacts with the hydroxyl group of the alloy oxide layer, forming strong bonds between the alloy and the initiator. Meanwhile, the α-bromo ester group at the other end initiates PMMA growth. Finally, ATRP polymerization takes place in the presence of a copper catalytic system.

FTIR spectrum analysis detected the absorption bands of PMMA grafted on Zn–Mg alloy, matching those in Ref. [26]. These include the asymmetric stretching of $CH_3$ at 2998 $cm^{-1}$, asymmetric and symmetric bonds of the methylene group ($CH_2$) at 2833 and 2949 $cm^{-1}$, carbonyl bond (C=O) at 1724 $cm^{-1}$, and the asymmetric stretching group of α-$CH_3$ at 1384 $cm^{-1}$ and 751 $cm^{-1}$.

Ensuring successful grafting in the small channels of the porous structure was crucial. Therefore, SEM/EDX analysis was conducted at the concave walls of these channels at the flattest parts (Fig. 4a–b). The grafted surface within the channels exhibited uniformity and some roughness. Elemental mapping of the channel walls, Fig. 4 (*c-f*), revealed a high C and medium O intensity but no evidence for Zn detection, indicating that the whole surface was effectively coated with PMMA.

Fig. 4g-l depicts polymer-coated alloys' cross-sectional morphology and the elemental mapping distribution. These images reveal the formation of a firmly adherent PMMA layer, serving as an interlayer between the polymer and the substrate, with no signs of delamination. The thickness of the PMMA layer measures 2.1 $\pm$ 0.4 μm (Fig. 4h), falling within the range reported in Ref. [26]. Furthermore, an EDX area analysis of the coated surface reveals the presence of the organic components C and O, demonstrating the existence of the polymer (Fig. 4i-l).

### 3.4. Corrosion performance

The corrosion performance of both bare and PMMA-grafted surfaces was assessed using electrochemical tests in SBF. Tafel extrapolating the potentiodynamic polarization curves (Fig. 5a) provided different electrochemical parameters. The results indicated a reduced corrosion current density ($I_{corr}$ = 9.4E-06 $\pm$ 6E-06 mA/$cm^2$) and higher potential ($E_{corr}$ = $-0.8 \pm 0.1$ V) after PMMA grafting compared to the bare surface ($I_{corr}$ = 4.5E-04 $\pm$ 5.7E-04 mA/$cm^2$ and $E_{corr}$ = $-1.3 \pm 0.4$ V). Since the $I_{corr}$ directly guides the reaction activity and thus the degradation rate, the lower $I_{corr}$ of the PMMA grafted surface consequently indicates a lower affinity to degradation. All potentiodynamic polarization curves of the PMMA-grafted surface exhibited a distinct plateau region in the anodic branch at an $I_{corr}$ of 4.9E-05 $\pm$ 4.4E-05 mA/$cm^2$. The PMMA protective layer is believed to break down at this point, allowing $Cl^-$ ions to access the substrate and initiate metal dissolution.

EIS outcomes offer an additional understanding of the corrosion characteristics exhibited by the included samples. The Nyquist plots (depicted in Fig. 5b) are adjusted based on the model circuits illustrated in Fig. 5c. Similar to the physical system, the resistance $R_s$ corresponds to the resistance of the SBF. In the case of the coated sample, $R_1$ and $R_2$ signify resistances, while $C_1$ and $C_2$ denote the capacitances of the
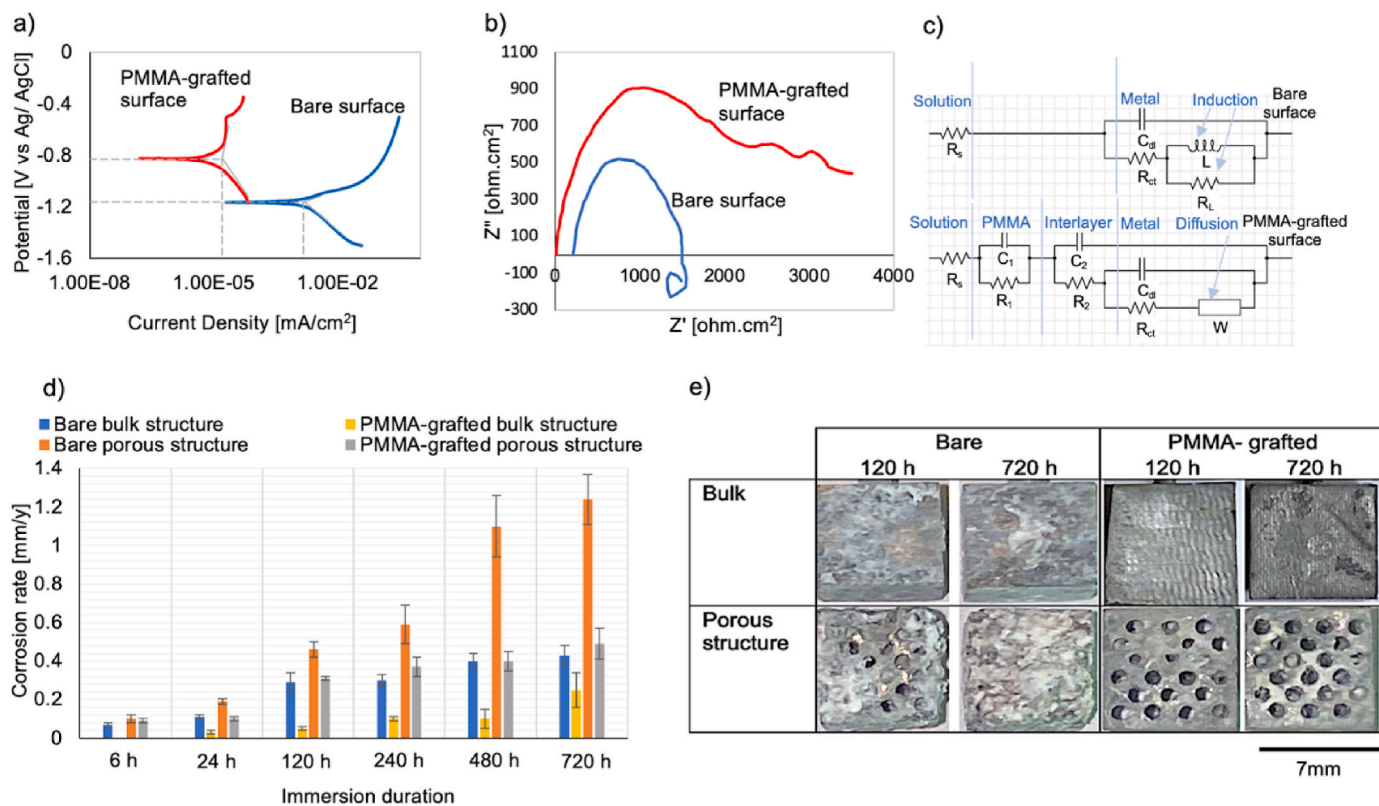


**Fig. 5.** Corrosion tests in SBF, where: a) polarization curves; (b) Nyquist plots; (c) schematic representation of the equivalent circuit used in (b); (d) corrosion rates calculated by the static immersion test and error bars represent the dispersion of the experimental values where n = 3 samples; and (e) the macroscopic surfaces of the samples after 120 h and 720 h of immersion.

PMMA layer and interlayer, respectively. Additionally, $R_{ct}$ represents charge transfer resistance, and $C_{dl}$ signifies the double-layer capacitance of the substrate.

The Nyquist plot of the bare surface can be described by a capacitive loop at the positive imaginary impedance (a semicircle at $Z'' > 0$), with a normalized diameter projection on $Z'$ equivalent to $R_{ct}$. Additionally, there is an inductive loop (curl-back) at negative imaginary impedance (a semicircle at $Z'' > 0$), indicative of the adsorption of intermediate ions on the metal surface. This inductive phenomenon is described by the parallel connection of inductance (L) and resistance (R) elements in the model circuit. On the other hand, the Nyquist plot of the coated surface exhibits a primary capacitive loop (a semicircle at $Z'' > 0$) with a normalized diameter projection on $Z'$ equivalent to $R_1$. Subsequently, there is a tendency to form multiple capacitive loops, each with normalized diameter projections on $Z'$ equivalent to $R_2$ and $R_{ct}$. Notably, the system includes the Warburg impedance to accommodate the diffusion phenomenon arising from surface heterogeneities [28].

The EIS results give rise to the $R_s$ and $R_{ct}$ for the bare surface, which have the values of $186.1 \pm 25.8 \ \Omega \ cm^2$ and $2017.8 \pm 531.2 \ \Omega \ cm^2$, respectively. For the PMMA-grafted surface, the Rs and $R_1$ are found to be equal to $35.7 \pm 27.0 \ \Omega \ cm^2$ and $3069.4 \pm 480.0 \ \Omega \ cm^2$, respectively.

The immersion test was conducted on both bare and PMMA-grafted
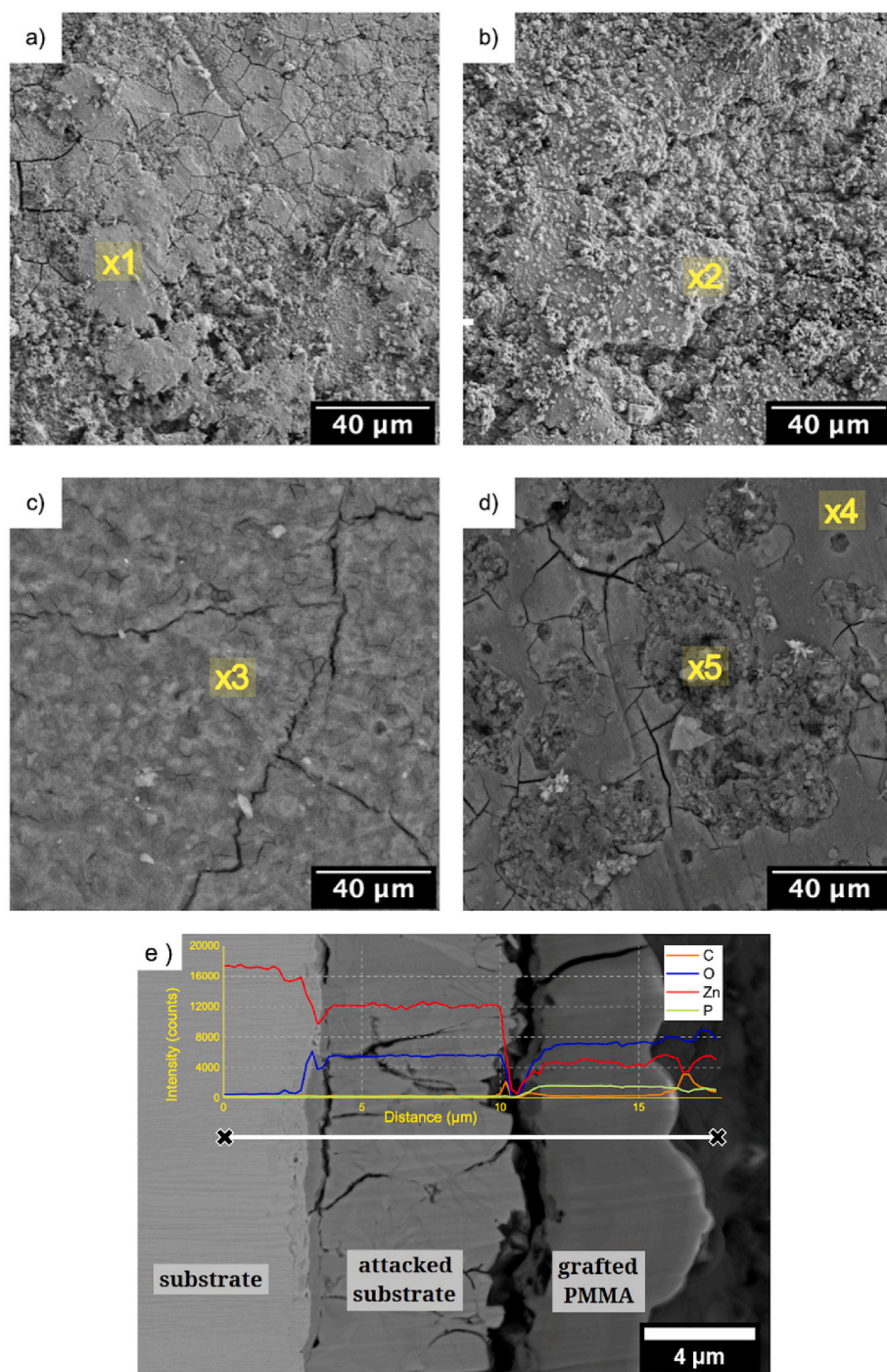


**Fig. 6.** Results of immersion test: (a–b) corrosion morphologies of bare surface, (c–d) corrosion morphologies of PMMA-grafted surfaces after immersion in SBF for 120 and 720 h, respectively. (e) Cross-section of the coated surface after immersion for 720 h.

**Table 2**
EDX analysis of the points in Fig. 6.

| Point | Elemental Composition (at.%) | | | | | | | | | |
|-------|------|-------|------|-------|------|------|------|------|------|-------|
|       | C    | O     | Br   | P     | K    | Ca   | Cl   | Na   | Mg   | Zn    |
| $x1$  | 0.3  | 62.26 | –    | 10.02 | 0.39 | 5.06 | –    | 4.93 | 0.21 | 12.74 |
| $x2$  | 0.16 | 37.75 | –    | 12.28 | –    | 2.14 | 1.25 | –    | 0.29 | 46.13 |
| $x3$  | 32.67| 23.03 | –    | 1.43  | –    | 2.2  | –    | –    | –    | 40.67 |
| $x4$  | 50.14| 39.06 | 0.04 | 2.31  | –    | 1.84 | –    | 0.76 | 0.05 | 5.8   |
| $x5$  | 14.9 | 19.41 | –    | –     | –    | –    | –    | –    | –    | 65.69 |

bulk and porous structures to monitor the evolution of corrosion behavior in SBF over different immersion durations: 6, 24, 120, 420, 480, and 720 h. The results of the immersion test are exhibited in Fig. 5d and **e**. The corrosion rate for the bare bulk surface was 0.3 mm/y and 0.4 mm/y after immersion for 120 and 720 h, respectively. After PMMA-grafting, these corrosion rates decreased to 0.05 and 0.3 mm/y, respectively. The porous structure exhibited a significantly higher corrosion rate than the bulk material. With a designed porosity of 65.8 %, the corrosion rate was approximately 58.6 % higher at 120 h and about 188.4 % higher at 720 h of immersion than the bulk material. However, PMMA grafting reduced the corrosion rate of the porous structure from 0.46 mm/y to 0.31 mm/y at 120 h and from 1.24 to 0.49 mm/y at 720 h of immersion.

The corroded surfaces after 120 and 720 h of immersion were investigated through the SEM/EDX analysis, as represented in Fig. 6a–d and Table 2. The SEM of the bare surface of the alloy after 120 h of immersion (Fig. 6a) reveals the presence of large islands surrounded by rough areas, with numerous cracks observed on the islands. Rough areas became predominant across most of the surface after extending the immersion duration to 720 h (Fig. 6b). Interestingly, the corrosion products detected on both surfaces were found to have nearly the same composition, as indicated by **points x1** and **x2.**

In contrast, the surface morphology of the PMMA-grafted sample after 120 h of immersion (depicted in Fig. 6c) shows the polymer layer covering the entire surface without any interruptions. However, wide, long cracks were uniformly dispersed. EDX analysis revealed high atomic percentages of the organic elements C and O, confirming the presence of the polymer layer. Additionally, EDX suggests the deposition of calcium phosphates and metallic ions from the substrate that have escaped through the cracks, as indicated by **point x3.**

The integrity of the coating after 720 h of immersion is debatable. Specifically, as depicted in Fig. 6d through SEM, there is evidence of partial peeling-off of the polymer. The areas where the polymer remains intact (designated as **point x4**) exhibit notably high C and O atomic percentages, along with minor amounts of Zn, Ca, P, Na, Mg, and Br, as indicated by EDX analysis. Conversely, the peeled-off regions exhibit heightened roughness, accompanied by cracks in the substrate and a significantly higher atomic percentage of Zn, coupled with lower atomic percentages of C and O (**point x5**). In summary, upon examination and comparison of the PMMA coating before and after immersion, it is evident that the polymer undergoes swelling and, in certain areas, peeling.

The corrosion mechanism of pure Zn and Zn–Mg alloys has been discussed previously [44]. It was concluded that two stages govern the corrosion process: the early stage, where $Cl^-$ ions attack strongly enough to destabilize the ZnO layer, forming the $ZnCl_2$ or $Zn_5(OH)_8Cl_2$ compounds, followed by a later stage, where Ca/P compound could be formed. In the current study, the Ca/P compounds are supposed to be formed on the bare surface of the alloy before 240 h of immersion (**points x1** and **x2**, Table 2). A notable reduction in the atomic proportions of Ca and P on the surface of the grafted polymer was observed after 120 h of immersion (**point x3**, Table 2), in contrast to the bare surface (**point x1**, Table 2). Despite this decrease, the Ca to P ratio was approximately 1.53, a value closely resembling the ratio found in HA. This alignment with the results of Barua [20] and Elakkiya [18] suggests

the potential for hydroxyapatite formation on the surface of the PMMA-based composite scaffold. The ability for the Ca/P compounds to be formed on a PMMA-graded surface after 720 h of immersion is significantly decreased. No Ca or P is detected on the surface of the substrate after PMMA peeling (point $x5$, Table 2), indicating an apparent inhibition of the corrosion process of the substrate. The assessment of the grafted polymer's thickness after 720 h of immersion involved a cross-sectional examination in SEM of the unpeeled sections (refer to Fig. 6e), and this thickness was compared to the pre-immersion state (Fig. 4g). In the cross-sectional view, polymer swelling was evident, leading to the PMMA thickness reaching $4.7 \pm 0.4$ μm, more than double the initial polymer thickness, with an observed break. Cracks within the polymer allowed penetration of the SBF), leading to crevice corrosion. A notable gap was observed between the attacked substrate (ZnO layer) and the PMMA. EDX analysis indicated minimal presence of Ca or P. Generally, the substrate layer beneath the PMMA exhibited a shallow localized attack at the interface, followed by a relatively deep inter-granular attack.

## 4. Discussion

### 4.1. Development of the mechanical and biodegradation behavior

Careful consideration should be given to the choice of heteroatoms to enhance the biomechanical properties of Zn alloy. According to the literature, the Zn alloying systems with Mg and Li emerge as the most promising candidates for achieving benchmark strength and corrosion performance values for biodegradable materials. Additionally, alloying Zn with Ag has shown potential for enhancing ductility, with an $E_f$ reaching up to 36 % [39–44]. However, it is essential to note that Li and Ag pose challenges as alloying elements for biodegradable materials. Excessive release of Li can lead to various physical and mental health issues, including congenital disabilities and bipolar disorder.

On the other hand, a high percentage of Ag must be added to Zn– Ag alloys to achieve superior strength and ductility, resulting in increased micro galvanic corrosion. In such cases, selective attacks within the solid solution may lead to the accumulation of $AgZn_3$ dendrites at the interface with implant tissue, potentially causing complications in tissue regeneration [42]. Therefore, in the current study, the comparison with existing literature focuses solely on the Zn–Mg alloying system, as depicted in Fig. 7a and **b**. In terms of mechanical performance, the benchmark YTS values should be in the range of 230–300 MPa, UTS between 300 and 400 MPa, and uniform elongation (beyond strain softening) should be approximately 10~20 % for orthopedic applications and exceed 20 % for cardiovascular applications. For biodegradable applications, benchmark corrosion rate values are typically set to be less than 350 μm/y for orthopedic applications and less than 20 μm/y for cardiovascular applications.

The attained microstructure of Zn-0.68 Mg could achieve one of the highest values of strength ($YTS_{0.2 \%} = 325.9$ MPa and UTS = 414.5 MPa) compared to other alloys with varying concentrations and preparation methods. However, better ductility could have been reached. High ductility can be achieved through severe plastic deformation (indicated by green points in Fig. 7a), resulting in smaller grain size. Alternatively, reducing the Mg content can enhance ductility by decreasing the volume
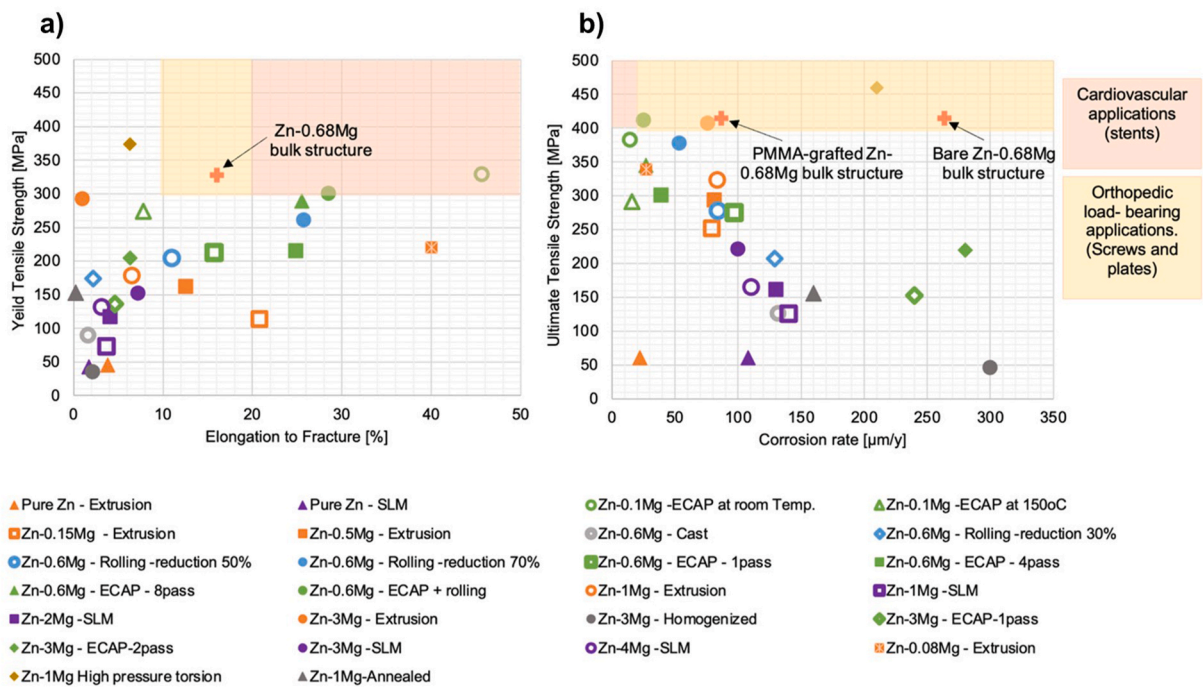
**Fig. 7.** Comparing the current study's tensile strengths, elongation, and corrosion with selected materials from the Zn–Mg system, (a) yield tensile strength vs. elongation to failure and (b) UTS vs. corrosion rate. Corrosion rates are calculated as the average corrosion of specimens immersed in SBF for 30 days or less [9,10, 37,45–49].
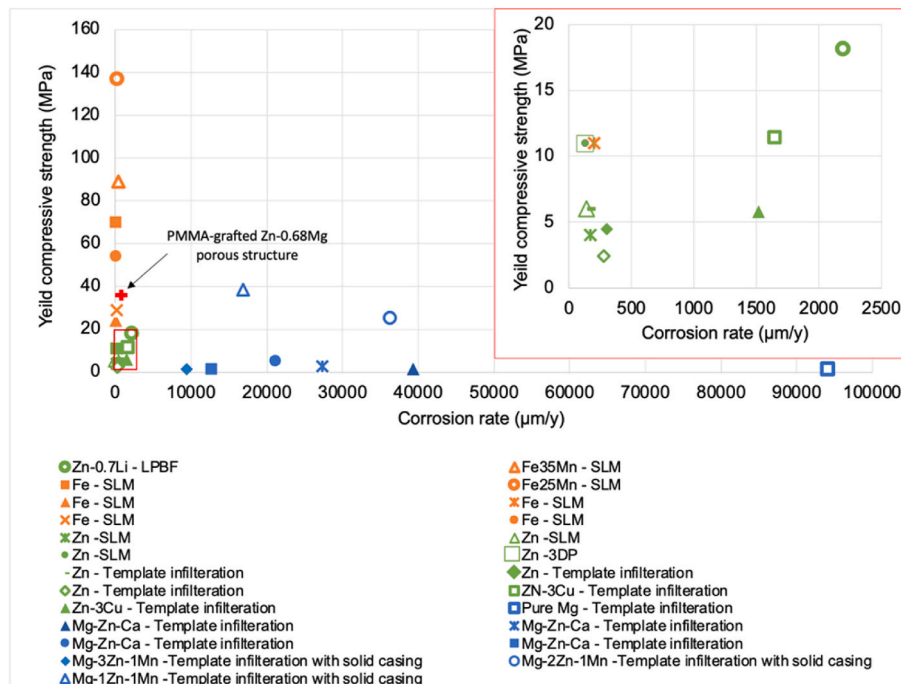


**Fig. 8.** Compressive yield strengths vs. corrosion rates of porous structures compared to selected porous structures in the literature. Corrosion rates are calculated as the average corrosion of specimens immersed in SBF for 30 days or less [50–57].

fraction of brittle, sharp-edged intermetallic phases, thereby reducing the likelihood of crack propagation. As indicated in Fig. 7b, the attained corrosion rate of the bare alloy falls in benchmark values for orthopedic applications, and it approaches those for cardiovascular applications with the application of a coating.

The perforated porous structure in the current study (67 % designed porosity obtained from as-extruded and PMMA-grafted Zn-0.68 Mg) exhibits higher compressive strength and corrosion resistance than Mg and Zn alloys. Furthermore, it is comparable to structures made from Fe, as shown in Fig. 8.

The porous structure in this study is primarily limited by its reliance on the milling perforation process. Although additive manufacturing is the most promising method for achieving orthopedic scaffold designs, studies in the literature regarding scaffolds of Zn alloys prepared by additive manufacturing.

### 4.2. Effect of microstructure features and texture on the mechanical performance

The one-pass extrusion of the Zn-0.68 Mg alloy, conducted at a relatively low temperature and a high reduction ratio, in conjunction with multiple phases, significantly promoted partial dynamic recrystallization of some grains. The bimodal grain structure consists of relatively large deformed grains and equiaxed sub-grains developed from LAGBs and HAGBs, resulting in relatively high tensile strength and satisfactory uniform elongation.

It is worth noting that the $MgZn_2$ phase was not detected in the present study of the as-extruded Zn-0.68 Mg alloy despite its rhombohedral crystallographic structure, which promotes its formation in the α-Zn matrix. In contrast, the detected $Mg_2Zn_{11}$ phase has a cubic structure, leading to significant lattice distortion energy within the hexagonal close-packed (hcp) α-Zn matrix, making the phase harder to form [58,59]. The non-detection of $MgZn_2$ may be attributed to the requirement for a higher Mg content within the Zn alloy to become discernible [60]. Alternatively, the $MgZn_2$ phase may exist at a tiny size, making it undetectable by XRD [38]. Another possibility is that the $MgZn_2$ is thermally unstable and diminishes during heat treatment and hot extrusion [61].

The observed bimodal grain structure is believed to result from forming the secondary phases after the alloy's solidification and extrusion. Notably, the sub-grains predominantly appear adjacent to these secondary phases, suggesting that dynamic recrystallization is more likely to occur in these areas (Fig. 2a, Region 1). At the beginning of the thermomechanical process, the secondary phases divide and localize the grain boundaries. As the deformation progresses, the strain increases, prompting fragmentation of the secondary phases. It is believed that at the interface between the secondary phases and the α-Zn solid solution, a considerable region characterized by high-density dislocations and a variation in crystallographic orientation is formed, resulting in the formation of the LAGBs. These LAGBs promote the formation of sub-grains [58]. Consequently, dislocation accumulation is absorbed, and the initiation of HAGBs occurs with the formation of new grains. The pinning effect of secondary phases and dislocations restrains the growth of sub-grains. The hardness variation and elasticity between the intermetallic phase and the α-Zn solid solution result in opposing strains throughout the deformation process. Activating various slip systems and dislocation tangling is favorable for dynamic recrystallization [37,39]. Ultimately, fully recrystallized sub-grains are thought to generate in-situ regions adjacent to secondary phases devoid of dislocations, as supported by Refs. [45,62]. The current study supports the same hypothesis, as evidenced by the nearly clear regions of the strain fields surrounding the sub-grains, even in the presence of secondary phases (Fig. 2e, Region 1). In contrast, the coarse grains containing precipitates exhibited high strain fields that are believed to be mainly due to dislocations (Fig. 2e, Region 2).

The strengthening mechanisms achieved through the extrusion of the Zn-0.68 Mg alloys involve grain boundary strengthening, intermetallic phase strengthening, and back stress strengthening. The involvement of solid solution strengthening is regarded as trivial because of the low solubility of Mg. The grain boundary strengthening is primarily governed by the Hall-Petch relationship but should be modified to account for the weighted contribution of both grains and sub-grains. The secondary phase strengthening accounts for the load transfer from the α-Zn solid solution and the $Mg_2Zn_{11}$ intermetallic, together with the dislocation-particle interaction directed by the Orowan formula. The back stress strength results from the difference in hardness between the grains and sub-grains and leads to tangling in the dislocation directions. The effectiveness of back stress strengthening is directly proportional to the strength of the texture of the relatively large grains [9,10,63]. The satisfactory ductility attained is believed to result from grain boundary sliding offered by the sub-grains with sizes smaller than 5 μm [40]. It is also suggested that the back stress work hardening works against the soft

hardening process, and consequently, a uniform elongation is achieved nearly till fracture [41]. The dislocations inside and outside the grains allowed slipping into being easier than cracks, and the twinning detected by the misorientation angle analysis, Fig. 2c and d, has contributed to liberating the stress concentrations caused by the difference in hardness between the α-Zn solid solution and the $Mg_2Zn_{11}$ phase thus the ductility increases. Additionally, texture weakening - achieved by dynamic recrystallization increases the chance of prismatic and pyramidal slip systems occurring, similar to the basal slip [59,64].

### 4.3. Effect of grafted-PMMA on Zn-0.68 Mg on the biodegradation performance

The microstructure of the alloy, characterized by a relatively low volume fraction of precipitates, induced uniform and intergranular corrosion. Very rare microgalvanic corrosion was detected between the α-Zn solid solution and the $Mg_2Zn_{11}$ secondary phase. It was observed that PMMA grafted had a significant effect in retarding the corrosion by isolating the surface from the SBF. However, PMMA is considered a hydrophilic polymer with an intrinsic contact angle below 90°, and its wettability depends on its roughness and morphology [65]. It may provide hypotheses on localized interface degradation, particularly the plasticizing effect of water molecules and the predominance of $Cl^-$ ions in the SBF.

These factors induce internal stresses and instability within the PMMA [66,67]. The degradation of the polymer-metal interface, as illustrated in Fig. 6e–is attributed to the formation of channels on the swollen PMMA, which leads to internal tensions and resulting fractures. It is essential to highlight that $Cl^-$ ions are a primary contributing factor. Furthermore, this observed behavior aligns with the degradation mechanism proposed in Ref. [26] involving another binary zinc with a 1.89 wt% content of Mg.

The scenario of PMMA swelling and losing consistency could be confirmed by Barua [21], who studied the *in vitro* weight loss of a PMMA-based scaffold and found a 6.45 % decay resulting from 14.2 % swelling capacity. The current challenge lies in monitoring the swelling and collapsing of PMMA, as PMMA itself is not biodegradable or bioresorbable. Despite its extensive use in orthopedic applications such as tissue regeneration and local drug delivery over the past thirty years, our understanding of how the body eliminates PMMA by-products still needs to be improved. Reggente et al. [30] have demonstrated the biosafety of the initiator used to produce the PMMA coat in this study.

While PMMA finds widespread use in surgical settings, the long-term toxicity of the MMA monomer is not well-documented. A comprehensive review article provides detailed insights [68]. A study on rats, wherein MMA was administered orally through a stomach tube, established its biosafety. The permissible safe dose of MMA in the body was 9 g/kg, with no discernible changes observed in various organs, including the liver, kidneys, heart, spleen, brain, lungs, and guts [68]. These findings indicate low acute toxicity of orally applied MMA, which undergoes rapid hydrolysis by enzymes in blood serum and subsequent metabolism to less toxic substances, such as pyruvate, via the citric acid cycle [69]. Furthermore, the half-life of MMA in human blood ranges between 20 and 40 min [70].

### 5. Conclusions

This work investigated the mechanical properties and corrosion resistance of a Zn-0.68 Mg alloy, both in bulk form and as a porous structure. A bimodal grain structure with promising mechanical characteristics was achieved through partial dynamic recrystallization. The alloy exhibited a yield strength of 325.9 MPa, a UTS of 414.5 MPa, and an elongation to failure of 16.3 %. Furthermore, applying PMMA coating using the "grafting-from" technique significantly reduced corrosion rates in electrochemical and immersion tests, enhancing the material's biocompatibility. PMMA-grafted coating significantly reduced the

corrosion rate (bulk: 0.43 mm/y to 0.25 mm/y, porous: 0.81 mm/y to 0.49 mm/y) by lowering the corrosion current density. Notably, the PMMA coating acted as a temporary barrier, delaying degradation while allowing the Zn-0.68 Mg alloy to biodegrade in SBF. Future research may explore alternative polymer coatings and adjustments in alloy composition to expand the material's utility in load-bearing orthopedics and cardiovascular applications.

## Declaration of competing interest

## CRediT authorship contribution statement

**Alia A. Diaa:** Writing – original draft, Validation, Software, Investigation, Formal analysis, Conceptualization. **Nahed El-Mahallawy:** Writing – review & editing, Supervision, Resources, Project administration, Conceptualization. **Madiha Shoeib:** Investigation, Formal analysis, Data curation. **Flavien Mouillard:** Investigation, Data curation. **Tom Ferté:** Investigation, Formal analysis, Data curation. **Patrick Masson:** Writing – review & editing, Supervision, Resources, Methodology, Data curation, Conceptualization. **Adele Carradò:** Writing – review & editing, Validation, Supervision, Project administration, Methodology, Funding acquisition, Conceptualization.

## Acknowledgments

## References

[1] Y. Liu, Y. Zheng, X.H. Chen, J.A. Yang, H. Pan, D. Chen, et al., Fundamental theory of biodegradable metals—Definition, Criteria, and design, Adv. Funct. Mater. 29 (2019) 1805402, https://doi.org/10.1002/ADFM.201805402.

[2] J. Zhang, Y. Jiang, Z. Shang, B. Zhao, M. Jiao, W. Liu, et al., Biodegradable metals for bone defect repair: a systematic review and meta-analysis based on animal studies, Bioact. Mater. 6 (2021) 4027–4052, https://doi.org/10.1016/J.BIOACTMAT.2021.03.035.

[3] C.D. Berdanier, J.T. Dwyer, D. Heber, HANDBOOK of NUTRITION and FOOD: Third Edition. Handbook of Nutrition and Food, Third Edition, 2016, pp. 1–1093, https://doi.org/10.1201/B15294/HANDBOOK-NUTRITION-FOOD-DAVID-HEBER-JOHANNA-DWYER-CAROLYN-BERDANIER.

[4] G.L. Koons, M. Diba, A.G. Mikos, Materials design for bone-tissue engineering, Nat. Rev. Mater. 5 (5) (2020) 584–603, https://doi.org/10.1038/s41578-020-0204-2, 8 2020.

[5] L. Kong, Z. Heydari, G.H. Lami, A. Saberi, M.S. Baltatu, P. Vizureanu, A comprehensive review of the current research Status of biodegradable zinc alloys and composites for biomedical applications, Materials 16 (2023) 4797, https://doi.org/10.3390/MA16134797, 2023;16:4797.

[6] H. Jin, S. Zhao, R. Guillory, P.K. Bowen, Z. Yin, A. Griebel, et al., Novel high-strength, low-alloys Zn-Mg (< 0.1 wt% Mg) and their arterial biodegradation, Mater. Sci. Eng. C 84 (2018) 67–79, https://doi.org/10.1016/J.MSEC.2017.11.021.

[7] C. Li, T. Huang, Z. Liu, Effects of thermomechanical processing on microstructures, mechanical properties, and biodegradation behaviour of dilute Zn–Mg alloys, J. Mater. Res. Technol. 23 (2023) 2940–2955, https://doi.org/10.1016/J.JMRT.2023.01.203.

[8] W. Liu, C. Zhang, P. Guo, Q. Shi, H. Feng, S. Zhang, et al., Achieving enhanced mechanical properties in the Mg–Y–Zn–V alloy by refining grains and improving the morphology and distribution of LPSO via pre-forging and subsequent rolling, J. Mater. Res. Technol. 29 (2024) 2493–2504, https://doi.org/10.1016/J.JMRT.2024.01.271.

[9] L. Ye, H. Liu, C. Sun, X. Zhuo, J. Ju, F. Xue, et al., Achieving high strength, excellent ductility, and suitable biodegradability in a Zn-0.1Mg alloy using room-temperature ECAP, J. Alloys Compd. 926 (2022) 166906, https://doi.org/10.1016/J.JALLCOM.2022.166906.

[10] R. Li, Y. Ding, H. Zhang, J. Lei, Y. Shen, Effective strengthening and toughening in Zn–1Mg alloy with bimodal grain structure achieved by conventional extrusion, Mater. Sci. Eng., A 854 (2022) 143850, https://doi.org/10.1016/J.MSEA.2022.143850.

[11] D. Lou, L. Wang, Y. Ren, H. Li, G. Qin, Textural evolution and improved ductility in Zn-0.2Mg-0.8Mn (wt%) alloys at different extrusion temperatures, J. Alloys Compd. 860 (2021) 158530, https://doi.org/10.1016/J.JALLCOM.2020.158530.

[12] J. Venezuela, M.S. Dargusch, The influence of alloying and fabrication techniques on the mechanical properties, biodegradability and biocompatibility of zinc: a comprehensive review, Acta Biomater. 87 (2019) 1–40, https://doi.org/10.1016/J.ACTBIO.2019.01.035.

[13] M.A.X. chun, J.I.N.S. yuan, W.U.R. zhi, W.A.N.G.J. xiu, G xiang Wang, B. Krit, et al., Corrosion behavior of Mg−Li alloys: a review, Trans. Nonferrous Metals Soc. China 31 (2021) 3228–3254, https://doi.org/10.1016/S1003-6326(21)65728-X.

[14] J. He, B. Jiang, J. Xu, J. Zhang, X. Yu, B. Liu, et al., Effect of texture symmetry on mechanical performance and corrosion resistance of magnesium alloy sheet, J. Alloys Compd. 723 (2017) 213–224, https://doi.org/10.1016/J.JALLCOM.2017.06.269.

[15] Y. Li, P. Pavanram, J. Zhou, K. Lietaert, P. Taheri, W. Li, et al., Additively manufactured biodegradable porous zinc, Acta Biomater. 101 (2020) 609–623, https://doi.org/10.1016/J.ACTBIO.2019.10.034.

[16] D. Xia, Y. Qin, H. Guo, P. Wen, H. Lin, M. Voshage, et al., Additively manufactured pure zinc porous scaffolds for critical-sized bone defects of rabbit femur, Bioact. Mater. 19 (2023) 12–23, https://doi.org/10.1016/J.BIOACTMAT.2022.03.010.

[17] M. Alizadeh-Osgouei, Y. Li, C. Wen, A comprehensive review of biodegradable synthetic polymer-ceramic composites and their manufacture for biomedical applications, Bioact. Mater. 4 (2019) 22–36, https://doi.org/10.1016/J.BIOACTMAT.2018.11.003.

[18] R. Oriňaková, R. Gorejová, Z.O. Králová, A. Oriňak, Surface modifications of biodegradable metallic Foams for Medical applications, Coatings 10 (2020) 819, https://doi.org/10.3390/COATINGS10090819, 2020;10:819.

[19] K. Elakkiya, P. Bargavi, S. Balakumar, 3D interconnected porous PMMA scaffold integrating with advanced nanostructured CaP-based biomaterials for rapid bone repair and regeneration, J. Mech. Behav. Biomed. Mater. 147 (2023) 106106, https://doi.org/10.1016/J.JMBBM.2023.106106.

[20] T.A.G. van Vugt, J.J. Arts, J.A.P. Geurts, Antibiotic-loaded polymethylmethacrylate beads and spacers in treatment of orthopedic infections and the role of biofilm formation, Front. Microbiol. 10 (2019), https://doi.org/10.3389/FMICB.2019.01626.

[21] E. Barua, A.B. Deoghare, S. Chatterjee, P. Sapkal, Effect of ZnO reinforcement on the compressive properties, in vitro bioactivity, biodegradability and cytocompatibility of bone scaffold developed from bovine bone-derived HAp and PMMA, Ceram. Int. 45 (2019) 20331–20345, https://doi.org/10.1016/J.CERAMINT.2019.07.006.

[22] R. Jayaram, P.W. O'Donnell, D.A. Puleo, Systems for local, sustained release of zoledronic acid as a potential treatment for metastatic bone disease, Mater. Sci. Eng. C 118 (2021) 111395, https://doi.org/10.1016/J.MSEC.2020.111395.

[23] S.R. Son, N.T.B. Linh, H.M. Yang, B.T. Lee, In vitro and in vivo evaluation of electrospun PCL/PMMA fibrous scaffolds for bone regeneration, Sci. Technol. Adv. Mater. 14 (2013) 15009–15019, https://doi.org/10.1088/1468-6996/14/1/015009.

[24] W. Jin, Q. Hao, X. Peng, P.K. Chu, Enhanced corrosion resistance and biocompatibilty of PMMA-coated ZK60 magnesium alloy. https://doi.org/10.1016/j.matlet.2016.03.071, 2016.

[25] O. Majumder, A.K. Singh Bankoti, T. Kaur, A. Thirugnanam, A.K. Mondal, The influence of silane and silane–PMMA coatings on the in vitro biodegradation behavior of AE42 magnesium alloy for cardiovascular stent applications, RSC Adv. 6 (2016) 107344–107354, https://doi.org/10.1039/C6RA23384H.

[26] A.A. Diaa, N. El-Mahallawy, M. Shoeib, N. Lallemand, F. Mouillard, P. Masson, et al., Effect of Mg addition and PMMA coating on the biodegradation behaviour of extruded Zn material, Materials 16 (2023) 707, https://doi.org/10.3390/MA16020707, 2023;16:707.

[27] M. Reggente, P. Masson, C. Dollinger, H. Palkowski, S. Zafeiratos, L. Jacomine, et al., Novel alkali activation of titanium substrates to grow thick and covalently bound PMMA layers, ACS Appl. Mater. Interfaces 10 (2018) 5967–5977, https://doi.org/10.1021/ACSAMI.7B17008/SUPPL_FILE/AM7B17008_SI_001.PDF.

[28] T. Schott, F. Liautaud, S. Kriegel, J. Faerber, W. He, P. Masson, et al., Stability of PMMA-grafted/Ti hybrid biomaterial interface in corrosive media, Pure Appl. Chem. 91 (2019) 1617–1629, https://doi.org/10.1515/PAC-2018-1218/MACHINEREADABLECITATION/RIS.

[29] M. Reggente, S. Kriegel, W. He, P. Masson, G. Pourroy, F. Mura, et al., How alkali-activated Ti surfaces affect the growth of tethered PMMA chains: a close-up study on the PMMA thickness and surface morphology, Pure Appl. Chem. (2019), https://doi.org/10.1515/PAC-2019-0223/PDF.

[30] M. Reggente, M. Harhash, S. Kriegel, P. Masson, J. Faerber, G. Pourroy, et al., Resin-free three-layered Ti/PMMA/Ti sandwich materials: adhesion and formability study, Compos. Struct. 218 (2019) 107–119, https://doi.org/10.1016/J.COMPSTRUCT.2019.03.039.

[31] Springer Handbook of Mechanical Engineering - Google Books n.d. https://www.google.com.eg/books/edition/Springer_Handbook_of_Mechanical_Engineer/9T5kd-ewRE8C?hl=fr&gbpv=1&dq=ASTM+RE8+E9+Mechanical+testing&pg=PA121&printsec=frontcover (accessed June 21, 2023).

[32] E8/E8M standard test methods for tension testing of metallic materials n.d. https://www.astm.org/e0008_e0008m-08.html. (Accessed 20 May 2023).

[33] E9 standard test methods of compression testing of metallic materials at room temperature (withdrawn 2009) n.d. https://www.astm.org/e0009-89ar00.html. (Accessed 20 May 2023).

[34] T. Kokubo, H. Takadama, How useful is SBF in predicting in vivo bone bioactivity? Biomaterials 27 (2006) 2907–2915, https://doi.org/10.1016/J.BIOMATERIALS.2006.01.017.

[35] Robert Baboian, Corrosion Tests and Standards: Application and Interpretation - Google Livres, ASTM International, 2005, p. 882.

[36] G31 standard practice for laboratory immersion corrosion testing of metals n.d. https://www.astm.org/g0031-72r04.html. (Accessed 21 June 2023).

[37] N. Mollaei, S.H. Razavi, M.R. Aboutalebi, S.M. Fatemi, Effect of Mn addition on the microstructure, mechanical, and corrosion properties of an extruded biodegradable Zn-0.2Mg alloy, J. Mater. Res. Technol. 22 (2023) 1983–1998, https://doi.org/10.1016/J.JMRT.2022.12.049.

[38] I. Minet, J. Delhalle, L. Hevesi, Z. Mekhalif, Surface-initiated ATRP of PMMA, PS and diblock PS-b-PMMA copolymers from stainless steel modified by 11-(2-bromoisobutyrate)-undecyl-1-phosphonic acid, J. Colloid Interface Sci. 332 (2009) 317–326, https://doi.org/10.1016/J.JCIS.2008.12.066.

[39] X. Zhuo, Y. Wu, J. Ju, H. Liu, J. Jiang, Z. Hu, et al., Recent progress of novel biodegradable zinc alloys: from the perspective of strengthening and toughening, J. Mater. Res. Technol. 17 (2022) 244–269, https://doi.org/10.1016/J.JMRT.2022.01.004.

[40] Y. Zhang, Y. Yan, X. Xu, Y. Lu, L. Chen, D. Li, et al., Investigation on the microstructure, mechanical properties, in vitro degradation behavior and biocompatibility of newly developed Zn-0.8%Li-(Mg, Ag) alloys for guided bone regeneration, Mater. Sci. Eng. C 99 (2019) 1021–1034, https://doi.org/10.1016/J.MSEC.2019.01.120.

[41] H. Huang, G. Li, Q. Jia, D. Bian, S. Guan, O. Kulyasova, et al., Recent advances on the mechanical behavior of zinc based biodegradable metals focusing on the strain softening phenomenon, Acta Biomater. 152 (2022) 1–18, https://doi.org/10.1016/J.ACTBIO.2022.08.041.

[42] M. Wątroba, K. Mech, W. Bednarczyk, J. Kawałko, M. Marciszko-Wiąckowska, M. Marzec, et al., Long-term in vitro corrosion behavior of Zn-3Ag and Zn-3Ag-0.5Mg alloys considered for biodegradable implant applications, Mater. Des. 213 (2022) 110289, https://doi.org/10.1016/J.MATDES.2021.110289.

[43] H. Yang, B. Jia, Z. Zhang, X. Qu, G. Li, W. Lin, et al., Alloying design of biodegradable zinc as promising bone implants for load-bearing applications, Nat. Commun. 11 (11) (2020) 1–16, https://doi.org/10.1038/s41467-019-14153-7, 1 2020.

[44] E. Mostaed, M. Sikora-Jasinska, J.W. Drelich, M. Vedani, Zinc-based alloys for degradable vascular stent applications, Acta Biomater. 71 (2018) 1, https://doi.org/10.1016/J.ACTBIO.2018.03.005.

[45] C. Ji, A. Ma, J. Jiang, H. Wu, H. Liu, S. Guo, et al., Regulating mechanical properties and degradation behavior of biodegradable Zn–0.6Mg alloy via ECAP plus cold rolling, J. Alloys Compd. 937 (2023), https://doi.org/10.1016/J.JALLCOM.2022.168487.

[46] M.S. Dambatta, S. Izman, D. Kurniawan, H. Hermawan, Processing of Zn-3Mg alloy by equal channel angular pressing for biodegradable metal implants, J. King Saud Univ. Sci. 29 (2017) 455–461, https://doi.org/10.1016/J.JKSUS.2017.07.008.

[47] N. Martynenko, N. Anisimova, O. Rybalchenko, M. Kiselevskiy, G. Rybalchenko, N. Tabachkova, et al., Structure, biodegradation, and in vitro bioactivity of Zn–1% Mg alloy strengthened by high-pressure torsion, Materials 15 (2022), https://doi.org/10.3390/MA15249073.

[48] Y. Yang, F. Yuan, C. Gao, P. Feng, L. Xue, S. He, et al., A combined strategy to enhance the properties of Zn by laser rapid solidification and laser alloying, J. Mech. Behav. Biomed. Mater. 82 (2018) 51–60, https://doi.org/10.1016/J.JMBBM.2018.03.018.

[49] J. Kubásek, D. Vojtěch, E. Jablonská, I. Pospíšilová, J. Lipov, T. Ruml, Structure, mechanical characteristics and in vitro degradation, cytotoxicity, genotoxicity and mutagenicity of novel biodegradable Zn–Mg alloys, Mater. Sci. Eng. C 58 (2016) 24–35, https://doi.org/10.1016/J.MSEC.2015.08.015.

[50] Y. Qin, H. Yang, A. Liu, J. Dai, P. Wen, Y. Zheng, et al., Processing optimization, mechanical properties, corrosion behavior and cytocompatibility of additively manufactured Zn-0.7Li biodegradable metals, Acta Biomater. 142 (2022) 388–401, https://doi.org/10.1016/J.ACTBIO.2022.01.049.

[51] D. Carluccio, C. Xu, J. Venezuela, Y. Cao, D. Kent, M. Bermingham, et al., Additively manufactured iron-manganese for biodegradable porous load-bearing bone scaffold applications, Acta Biomater. 103 (2020) 346–360, https://doi.org/10.1016/J.ACTBIO.2019.12.018.

[52] C. Shuai, W. Yang, Y. Yang, H. Pan, C. He, F. Qi, et al., Selective laser melted Fe-Mn bone scaffold: microstructure, corrosion behavior and cell response, Mater. Res. Express 7 (2020) 015404, https://doi.org/10.1088/2053-1591/AB62F5.

[53] Y. Li, H. Jahr, P. Pavanram, F.S.L. Bobbert, U. Puggi, X.Y. Zhang, et al., Additively manufactured functionally graded biodegradable porous iron, Acta Biomater. 96 (2019) 646–661, https://doi.org/10.1016/J.ACTBIO.2019.07.013.

[54] I. Cockerill, Y. Su, S. Sinha, Y.X. Qin, Y. Zheng, M.L. Young, et al., Porous zinc scaffolds for bone tissue engineering applications: a novel additive manufacturing and casting approach, Mater. Sci. Eng. C 110 (2020) 110738, https://doi.org/10.1016/J.MSEC.2020.110738.

[55] Y. Hou, G. Jia, R. Yue, C. Chen, J. Pei, H. Zhang, et al., Synthesis of biodegradable Zn-based scaffolds using NaCl templates: relationship between porosity, compressive properties and degradation behavior, Mater. Char. 137 (2018) 162–169, https://doi.org/10.1016/J.MATCHAR.2018.01.033.

[56] J. Asadi, B. Korojy, S.A. Hosseini, M. Alishahi, Effect of cell structure on mechanical and bio-corrosion behavior of biodegradable Mg-Zn-Ca foam, Mater. Today Commun. 28 (2021) 102715, https://doi.org/10.1016/J.MTCOMM.2021.102715.

[57] X.Z. Lu, C.P. Lai, L.C. Chan, Novel design of a coral-like open-cell porous degradable magnesium implant for orthopaedic application, Mater. Des. 188 (2020) 108474, https://doi.org/10.1016/J.MATDES.2020.108474.

[58] T.A. Vida, C. Brito, T.S. Lima, J.E. Spinelli, N. Cheung, A. Garcia, Near-eutectic Zn-Mg alloys: interrelations of solidification thermal parameters, microstructure length scale and tensile/corrosion properties, Curr. Appl. Phys. 19 (2019) 582–598, https://doi.org/10.1016/J.CAP.2019.02.013.

[59] Z. Li, Z.Z. Shi, H.J. Zhang, H.F. Li, Y. Feng, L.N. Wang, Hierarchical microstructure and two-stage corrosion behavior of a high-performance near-eutectic Zn-Li alloy, J. Mater. Sci. Technol. 80 (2021) 50–65, https://doi.org/10.1016/J.JMST.2020.10.076.

[60] T. Prosek, A. Nazarov, U. Bexell, D. Thierry, J. Serak, Corrosion mechanism of model zinc–magnesium alloys in atmospheric conditions, Corrosion Sci. 50 (2008) 2216–2231, https://doi.org/10.1016/J.CORSCI.2008.06.008.

[61] L. Ye, H. Huang, C. Sun, X. Zhuo, Q. Dong, H. Liu, et al., Effect of grain size and volume fraction of eutectic structure on mechanical properties and corrosion behavior of as-cast Zn–Mg binary alloys, J. Mater. Res. Technol. 16 (2022) 1673–1685, https://doi.org/10.1016/J.JMRT.2021.12.101.

[62] M. Gao, K. Yang, L. Tan, Z. Ma, Role of bimodal-grained structure with random texture on mechanical and corrosion properties of a Mg-Zn-Nd alloy, J. Magnesium Alloys 10 (2022) 2147–2157, https://doi.org/10.1016/J.JMA.2021.03.024.

[63] X. Zhuo, W. Gao, L. Zhao, S. Zhao, H. Liu, Z. Hu, et al., A bimodal grain structured Zn-0.4Mg-0.02Mn alloy with superior strength-ductility synergy, Mater. Sci. Eng., A 862 (2023) 144514, https://doi.org/10.1016/J.MSEA.2022.144514.

[64] M. Li, X. Wang, Y. Liu, Z. Xiao, Y. Huang, Heterogeneous bimodal microstructure and its formation mechanism of Mg-Gd-Y-Zn-Zr alloy during isothermal compression, J. Alloys Compd. 947 (2023) 169523, https://doi.org/10.1016/J.JALLCOM.2023.169523.

[65] Y. Ma, X. Cao, S. Feng, Y. Ma, H. Zou, Fabrication of super-hydrophobic film from PMMA with intrinsic water contact angle below 90, Polymer (Guildf) 48 (2007) 7455–7460, https://doi.org/10.1016/J.POLYMER.2007.10.038.

[66] L. Chen, Y. Tang, K. Zhao, J. Liu, X. Jiang, Y. Sun, et al., High water-absorbent and fast-expanding PMMA bone cement with double-bridged structure, J. Appl. Polym. Sci. 138 (2021) 50464, https://doi.org/10.1002/APP.50464.

[67] M. N'Diaye, F. Pascaretti-Grizon, P. Massin, M.F. Baslé, D. Chappard, Water absorption of poly(methyl methacrylate) measured by vertical interference microscopy, Langmuir 28 (2012) 11609–11614, https://doi.org/10.1021/LA302260A/ASSET/IMAGES/MEDIUM/LA-2012-02260A_0007.GIF.

[68] P.A. Leggat, D.R. Smith, U. Kedjarune, Surgical applications of methyl methacrylate: a review of toxicity, Arch. Environ. Occup. Health 64 (2009) 207–212, https://doi.org/10.1080/19338240903241291.

[69] Z. Bereznowski, In vivo assessment of methyl methacrylate metabolism and toxicity, Int. J. Biochem. Cell Biol. 27 (1995) 1311–1316, https://doi.org/10.1016/1357-2725(95)00101-T.

[70] J.A. Corkill, E.J. Lloyd, P. Hoyle, D.H.G. Crout, R.S.M. Ling, M.L. James, et al., Toxicology of methyl methacrylate: the rate of disappearance of methyl methacrylate in human blood in vitro, Clin. Chim. Acta 68 (1976) 141–146, https://doi.org/10.1016/0009-8981(76)90413-7.